PAPER

On variable stiffness of flexible parallel electroadhesive structures

IOP Publishing Smart Materials and Structures
Smart Mater. Struct. **32** (2023) 055004 (12pp) https://doi.org/10.1088/1361-665X/acbd01

On variable stiffness of flexible parallel electroadhesive structures

Yingze Yuan[1,4], Fengfeng Li[1,4], Jianglong Guo[2], Liwu Liu[1,*], Yanju Liu[1,*] and Jinsong Leng[3]

[1] Department of Astronautical Science and Mechanics, Harbin Institute of Technology, Harbin 150001, People's Republic of China
[2] School of Science, Harbin Institute of Technology (Shenzhen), Shenzhen 518055, People's Republic of China
[3] Center for Composite Materials and Structures, Harbin Institute of Technology, Harbin 150080, People's Republic of China

E-mail: liuliwu_006@163.com and yj_liu@hit.edu.cn

Received 17 August 2022, revised 27 January 2023
Accepted for publication 16 February 2023
Published 23 March 2023

Abstract

Electrostatic layer jamming represents a lightweight, low energy consumption, electrically tunable, and cost-effective variable stiffness structure. Flexible parallel electroadhesive structures are the simplest form of electrostatic layer jamming. There is a lack of comprehensive and experimentally validated theoretical variable stiffness models of flexible parallel electroadhesive structures. Here we present the first variable stiffness model of flexible parallel electroadhesive structures under three-point bending, cantilever beam bending subjected to tip concentrated forces, and cantilever beam bending subjected to uniformly distributed forces, using the Euler–Bernoulli beam theory and considering friction and slip between layers by integrating the Maxwell stress tensor into the model. We find that: (1) three-point bending and cantilever beam bending under tip concentrated forces only have pre-slip and full-slip, whereas cantilever beam bending under uniformly distributed forces has an additional partial-slip which can be used for stiffness modulation; (2) the stiffness during the pre-slip stage is four times larger than the stiffness in the full-slip stage; and (3) increasing the voltage, dielectric permittivity, and coefficient of friction can elongate the pre-slip stage, thus enhancing the structural load capability. A customized three-point bending and a cantilever beam bending experimental setup were developed and the experimental deflection–force curve agreed relatively well with the theoretical one. The model, which considered electrode thickness and Young's modulus, and the results presented in this work are useful insights for understanding the variable stiffness mechanism of electroadhesive layer jamming and are helpful for their structural optimization towards practical applications.

Supplementary material for this article is available online

Keywords: variable stiffness, electroadhesion, Euler–Bernoulli beam theory, Maxwell stress tensor, layer slip

(Some figures may appear in colour only in the online journal)

[4] These authors contributed equally to the work.
[*] Authors to whom any correspondence should be addressed.

1. Introduction

Variable stiffness materials and structures [1–4] are ubiquitous in nature and our daily life. In nature, animals use their excellent variable stiffness capabilities to survive and adapt in unknown and changing environments. Their muscles use soft states to achieve necessary compliance and stiffened states for load bearing. In daily life, common variable stiffness materials include phase change materials and rheological materials [1–4]. Phase change materials employ either solid/liquid phase change (such as melting) or glass transition, subjected to external stimuli such as temperature, electric field, and magnetic field, to realize stiffness tuning [3–5]. Low melting point materials are a major phase change material, including wax and low melting point alloy [5, 6]. Rheological materials use external electric or magnetic fields to modulate their rheological properties such as viscosity and stiffness to realize stiffness changing [3, 4]. Electrorheological/magnetorheological fluids/elastomers are major rheological materials. Variable stiffness structures mainly use jamming (pressure or force driven friction tuning) [1–4, 7] to realize stiffness modulation and jamming structures include particle jamming [8, 9], layer jamming [10, 11], wire jamming [12], and fibre jamming [13].

Current variable stiffness materials and structures have their own strengths and weaknesses. Phase changes materials have large stiffness tuning ranges but they are slow in stiffness change and energy intensive [1–4]. Rheological materials are rapid in stiffness change but material properties tend to degrade over time [1–4]. Jamming structures are relatively easy-to-make and not difficult to be controlled but most require cumbersome and energy intensive pumps or motors [1–4]. Electrostatic layer jamming is a quiet, lightweight, low energy consumption, and electrically controllable variable stiffness structure [14].

Parallel electroadhesive structures, made of two layers (each having one electrode bonded to an insulating film), are the simplest form of electrostatic layer jamming. As shown in figure 1(a), under the weight of 20 g, the displacement of a customized-made parallel electroadhesive structure changed from 4.22 mm (under 0 kV) to 1.92 mm (under 1 kV), manifesting the bending stiffness change from 0.046 N mm^{-1} to 0.102 N mm^{-1}. Principle of the variable stiffness change can be seen in figure 1(b). When no voltage is applied the electrode, the friction force between two layers is relatively small and slip can easily occur, leading to large structure deformations under loads. When applying a voltage to the structure, the friction force increases due to electrostatic attractions between two layers, preventing the easy layer slip between layers thus leading to decreased deformations, i.e. larger bending stiffnesses.

Variable stiffness modelling of parallel electroadhesive structures is important to fundamentally understand their variable stiffness effect and optimize their structures for practical applications. Only a few papers have been published so far, as summarized and shown in table 1, where n is the number of layers, h is the layer thickness, b_f is the film width, E is the Young's modulus, U is the applied voltage,

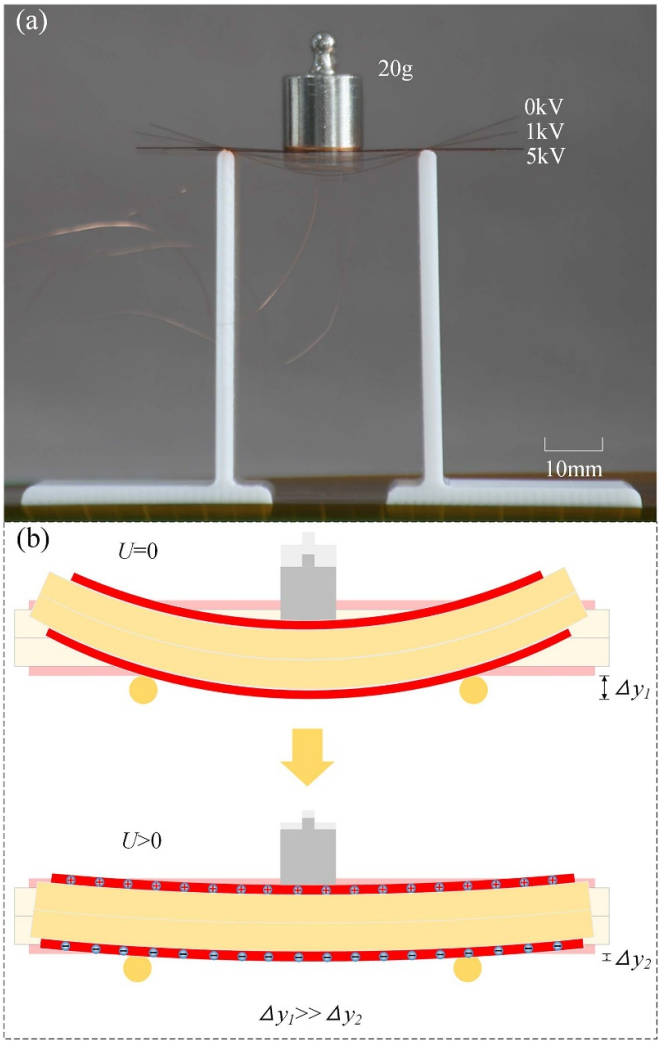

Figure 1. Variable stiffness of a flexible parallel electroadhesive: (a) a flexible parallel electroadhesive can change its bending stiffness under different voltages such as 1 and 5 kV, and (b) schematic diagram of the variable stiffness principle of flexible parallel electroadhesives, where red denotes the electrodes, yellow denotes the insulating materials, and gray denotes the 20 g load.

F is the load, α and β are related to the layer thickness, Young's modulus, Poisson's ratio, dielectric constant, relative dielectric constant, and structure length and width (the dimension of α is Time^(2)Mass^(−1) and the dimension of β is Time^(6)Length^(−7)), U_i is the deformation energy of the ith segment, L_f is the film length, H is the total thickness of the structure, w is the deflection of the structure, ε_0 is the dielectric constant of vacuum, ε_r is the relative dielectric constant of the film, b is the width of the electrode, and μ is the coefficient of friction.

Bergamini *et al* [15] studied the variable stiffness effect of a flexible multi-layer electrostatic layer jamming beam structure, subjected to tip concentrated forces, using the simple flexural rigidity equation (the product of Young's modulus and moment of inertia) to represent the structural stiffness, showing that stiffness change is the square of the number of layers. However, the square relationship was not validated and slip,

Table 1. Summary of existing variable stiffness models of parallel electroadhesive structures.

References	Stiffness representation method	Initial stiffness (under 0 V)	Maximum stiffness
[15]	Flexural rigidity equation	$n\frac{b_f h^3}{4{L_f}^3}E$	$n^3\frac{b_f h^3}{4{L_f}^3}E$
[16]	Quadratic integral of the differential equation of the deflection curve	$\frac{1}{\alpha}$	$\frac{F}{\alpha F+\beta U^2}$
[17]	Castigliano's second theorem	$\frac{F}{\frac{d}{dF}\sum_{i=1}^{5}U_i}$	$\frac{n^2F}{\frac{d}{dF}\sum_{i=1}^{5}U_i}$
[18]	Castigliano's first theorem	$\frac{16Eb_fH^3}{n^2{L_f}^3}$	$\frac{16Eb_fH^3}{n^2{L_f}^3}+\frac{\varepsilon_0\varepsilon_r n^2U^2b\mu}{wH}$

which is common in layer jamming, was not included in the model.

Imamura *et al* [16] studied the variable stiffness effect of a multi-layer dielectric elastomer actuator beam structure, subjected to tip concentrated forces, using an elastic model which essentially was a quadratic integral of the differential equation of the deflection curve. However, the theoretical shear electroadhesive stress results did not match well with the experimental results when the applied voltage was over 500 V and slip was not considered.

Henke and Gerlach [17] studied the variable stiffness effect of a five-segment multi-layer parallel electroadhesive beam structure subjected to tip concentrated forces, using the Castigliano's second theorem (which used deflections to represent the stiffness change). This work introduced the importance of considering slip between layers. However, the variable stiffness model of each segment was the same simple one used by Bergamini *et al* [15].

Tabata *et al* [18] studied the variable stiffness effect of a flexible multi-layer electrostatic layer jamming beam structure, subjected to central concentrated forces, using the Castigliano's first theorem (which used structural ultimate load capacities to represent the stiffness change). This work only presented the theoretical nonlinear relationship between force and deflection. Slip between layers was not considered. Also, the theoretical model was not experimentally validated.

Here we present the first variable stiffness model of flexible parallel electroadhesive structures. We consider the structure under three different cases: (1) three-point bending, (2) cantilever beam bending subjected to tip concentrated forces, and (3) cantilever beam bending subjected to uniformly distributed forces. We apply the Euler–Bernoulli beam theory and consider how the structural mechanical behaviour is influenced by electroadhesive pressure by integrating the Maxwell stress tensor into the model and interfacial friction and slip. The analytical modelling begins by setting the model and calculating the electroadhesive shear stress between layers. Stiffnesses of the three bending cases are then derived. Followed by this, theoretical results are shown, together with a customized three-point bending experimental setup and a cantilever beam bending experimental setup developed to validate the model. Conclusions and future work are finally given.

2. Analytical modelling

2.1. Problem definition

As aforementioned, stiffness modulation of electroadhesive jamming structures comes from varying the electroadhesive shear forces between layers by applying different voltages to the electrodes. Here we assume that: (1) electric fields are uniformly distributed between electrodes and the edge effect is not considered; and (2) the materials are linear, continuous, homogenous, and isotropic materials that satisfy linear elasticity and small deformation assumptions. We use the differential equation of the deflection curvature of electroadhesive jamming structure to establish the relationship between external loads and corresponding deflections, i.e. the governing equation:

$$\sum_{i=1}^{n} E_i I_i \kappa(x) = M(x) \tag{1}$$

where i is the number of a single-layer laminate, I is the second moment of area of a single-layer laminate about the neutral axis of the structure, $\kappa(x)$ is the curvature of the structure, and $M(x)$ is the bending moment of the structure.

When the structure is fully bonded using electroadhesion and can be regarded a whole laminate, the shear stress inside the structure is:

$$\tau(x,y) = \frac{F_S(x)S_z^*(y)}{bI_z} \tag{2}$$

where $F_S(x)$ is the shear force along the cross-section of the structure under a load and varies along the x-axis direction, I_z is the second moment of area of the whole laminate about the neutral axis of the structure, and $S_z^*(y)$ is a function of y, representing the first moment of area A^* (A^* is the area outside the desired shear stress point) about the neutral axis of the structure.

Here we set the neutral axis as the z axis, the expression of $S_z^*(y)$ can be written as $S_z^*(y) = \int_{A^*} y\mathrm{d}A$. The maximum static friction stress between layers provided by the interlayer adhesion caused by electrostatic forces is [19]:

$$\tau_f = \mu T \tag{3}$$

where T is the Maxwell stress tensor.

For a multi-layer structure, under the action of external forces, the position where the layers are in contact with each other will slip. We assume that when the multilayer structure is a whole laminate, the shear stress $\tau(x,y)$ will be generated at the position where the layers are in contact with each other. These shear stresses $\tau(x,y)$ can be regarded as the constraint stress required to maintain the structure as a whole, and they

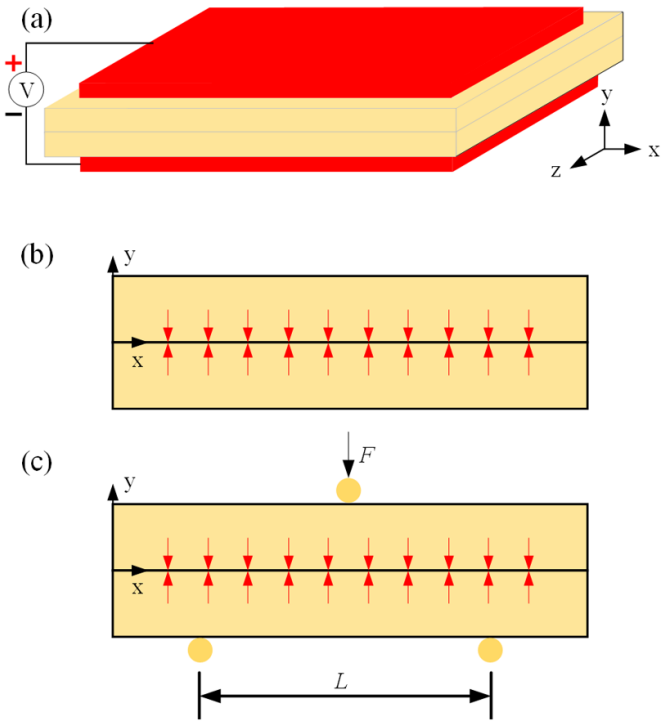

Figure 2. Schematic diagram of the variable stiffness flexible parallel electroadhesive physical model: (a) 3D configuration under no load, (b) 2D configuration under no load (red arrows denote electroadhesive forces), and (c) 2D configuration under a central concentrated force (F is the load and L is the three-point bending support span length).

are equal in value and opposite in direction. The maximum static friction stress provided by the electrostatic force mentioned in equation (3) can act as a constraining stress. When the maximum static friction stress is large enough, the structure can be maintained as a whole and ensure that the contact position between the layers does not slip. When the maximum static friction stress is not large enough, the structure will slip partially or even completely. We then have three phases during the structural bending:

(1) pre-slip or adhesion phase: when $\tau_{\max}(x,y) \leqslant \tau_f$, the whole structure is electrically bonded in a stable way;
(2) partial-slip or transition phase: when $\tau_{\min}(x,y) \leqslant \tau_f < \tau_{\max}(x,y)$, the whole structure has partial layer slips;
(3) full-slip phase: when $\tau_{\min}(x,y) > \tau_f$, layer slip occurs in the whole structure.

$\tau_{\max}(x,y)$ and $\tau_{\min}(x,y)$ represent the maximum and minimum shear stress at the position where the layers are in contact with each other respectively when we assume that the multilayer structure is a whole.

In this work, we study the simplest form of electrostatic layer jamming, as shown in figure 1, where $n = 2$, as shown in figure 2(a). We can use a simplified 2D model shown in figure 2(b) to represent the whole model.

When the upper and lower laminates are adhered together, the neutral axis of the structure is located in the position where the layers are in contact with each other and we set the neutral axis as the z axis. We then can get the shear stress at the position where the layers are in contact with each other as $\tau(x,0)$. Here we use $\tau_{\max}$ and $\tau_{\min}$ to replace $\tau_{\max}(x,0)$ and $\tau_{\min}(x,0)$, respectively, i.e. $\tau_{\max}$ and $\tau_{\min}$ represent the maximum and minimum shear stress on the contact surfaces of the upper and lower laminates, respectively.

In this work, we study the variable stiffness of flexible parallel electroadhesive structures under three-point bending (see figure 2(c)), cantilever beam bending subjected to tip concentrated forces, and cantilever beam bending subjected to uniformly distributed forces. The overall structural stiffness in each stage can be represented as:

$$k = -\frac{\partial F}{\partial w}. \tag{4}$$

We thus need to solve the following problems:

(1) Electroadhesive stresses under AC/DC voltages,
(2) Critical loads in the pre-slip stage and partial-slip stage,
(3) Critical loads in the partial-slip stage and full-slip stage,
(4) Bending stiffnesses of three stages.

2.2. Electroadhesive stress calculation

The Maxwell stress tensor is usually used to manifest the interaction between electromagnetic forces and mechanical momentum [20]: $T_{ij} = \varepsilon\left(E_iE_j - \frac{1}{2}\delta_{ij}E_{ij}^2\right) + \frac{1}{\mu_0}\left(B_iB_j - \frac{1}{2}\delta_{ij}B_{ij}^2\right)$, where ε is the dielectric permittivity, E_i/E_j is the electric field strength in the i/jth direction, B_i/B_j is the magnetic field strength in the i/jth direction, μ_0 is the vacuum permeability, and δ_{ij} is the Kronecker delta. Here we ignore the magnetic part, then we have:

$$\begin{aligned} T_{ij} &= \varepsilon\left(E_iE_j - \frac{1}{2}\delta_{ij}E_{ij}^2\right) \\ &= \varepsilon\begin{pmatrix} \frac{1}{2}\left(E_z^2 - E_x^2 - E_y^2\right) & E_xE_y & E_xE_z \\ E_yE_x & \frac{1}{2}\left(E_x^2 - E_z^2 - E_y^2\right) & E_yE_z \\ E_zE_x & E_zE_y & \frac{1}{2}\left(E_y^2 - E_z^2 - E_x^2\right) \end{pmatrix}, \end{aligned}$$

where $E_z/E_x/E_y$ is the electric field strength in the $z/x/y$ direction and $\varepsilon = \varepsilon_0\varepsilon_r$ (here we assume the voltage application frequency is below 10^{10} Hz, meaning that the dielectric loss can be ignored and dielectric constants can be used to denote dielectric permittivity).

Because the electric field is uniformly distributed, the Maxwell stress tensor in the y direction is:

$$T_{yy} = \frac{1}{2}\varepsilon_0\varepsilon_r E_y^2. \tag{5}$$

We then calculate the electric field strength under AC/DC voltage respectively. Under AC voltages, we have $\varepsilon_{\text{up}}E_{\text{up}} = \varepsilon_{\text{down}}E_{\text{down}}$ [21], where $\varepsilon_{\text{up}}/\varepsilon_{\text{down}}$ is the permittivity of upper/underlying insulating materials. As $E = \frac{U(t)}{d}$ and $U(t) = U(t)_{\text{up}} + U(t)_{\text{down}}$, where $U(t)_{\text{up}}/U(t)_{\text{down}}$ is the internal potential of the upper/underlying insulating materials, we can have: $E_{\text{up}} = \frac{\varepsilon_{\text{down}}}{\varepsilon_{\text{up}}d_{\text{down}} + \varepsilon_{\text{down}}d_{\text{up}}}U(t)$ and

$E_{\text{down}} = \frac{\varepsilon_{\text{up}}}{\varepsilon_{\text{up}} d_{\text{down}} + \varepsilon_{\text{down}} d_{\text{up}}} U(t)$. Here we set $\varepsilon_{\text{up}} = \varepsilon_{\text{down}} = \varepsilon_0 \varepsilon_r$, $d_{\text{up}} = d_{\text{down}} = h_f$, we can then obtain: $E_{\text{up}} = E_{\text{down}} = \frac{U(t)}{2h_f}$.

Under DC voltages, we have $\gamma_{\text{up}} E_{\text{up}} = \gamma_{\text{down}} E_{\text{down}}$ [21]. Similar to the derivation of the electric field under AC voltage, we can obtain $E_{\text{up}} = \frac{\gamma_{\text{down}}}{\gamma_{\text{up}} d_{\text{down}} + \gamma_{\text{down}} d_{\text{up}}} U$ and $E_{\text{down}} = \frac{\gamma_{\text{up}}}{\gamma_{\text{up}} d_{\text{down}} + \gamma_{\text{down}} d_{\text{up}}} U$. Here we set $\varepsilon_{\text{up}} = \varepsilon_{\text{down}} = \varepsilon_0 \varepsilon_r$, $d_{\text{up}} = d_{\text{down}} = h_f$, we can then obtain: $E_{\text{up}} = E_{\text{down}} = \frac{U}{2h_f}$.

We then have $E_y = \frac{U(t)}{2h_f}$ that can be used for both AC and DC cases. Equation (5), which is the electroadhesive stress, becomes: $T_{yy} = \frac{\varepsilon_0 \varepsilon_r U(t)^2}{8{h_f}^2}$. Then, the electroadhesive shear stress between layers is:

$$\tau_f = \mu T_{yy} = \frac{\mu \varepsilon_0 \varepsilon_r U(t)^2}{8{h_f}^2}. \tag{6}$$

2.3. Variable stiffness model of the three-point bending case

We firstly focus on the analytical modelling based on the boundary condition of central concentrated forces (see figure 2(c)) of three-point bending beams, where the span is L, the electrode length is L_e, the width is b, the thickness is h_e, the elastic modulus is E_e, the length of the insulating material is L_f, the width is b_f, the thickness is h_f, the elastic modulus is E_f, the friction coefficient is μ, and the relative permittivity is ε_r. In practice, the size of the insulating material is slightly larger than that of the electrode material for experimental safety. Due to the fact that the extra insulating material area is small and does not adhere together, then it has little impact on the model. In order to simplify the calculation, the length and width of the insulating material were set to be the same as the electrode material.

Please note that as we use flexible materials here, electroadhesive forces between films will change the coefficient of friction. It is therefore a must a measure the static coefficient of friction under the same voltage applied to the parallel flexible electroadhesive structure, and this coefficient can be determined by the ratio of the tangential electroadhesive force to the normal electroadhesive force. In order to determine whether the variable stiffness process of the three-point bending model has partial-slip or not, we need to introduce the shear stress calculation equation:

$$\tau_{yx} = \frac{F_S S_z^*}{b I_z} = \frac{3F}{8b(h_e + h_f)} \tag{7}$$

where τ_{yx} is the transverse shear stress in the x-direction perpendicular to the y-plane and we can see that the interlaminar shear stress of the model is constant.

As the interlaminar shear stress is constant, we have $\tau_{\min} = \tau_{\max} = \tau_{yx}$, then we can conclude that variable stiffness of three-point bending does not have partial-slip stages. When $\tau_{yx} \leqslant \tau_f$, the structure is completely adhered together and should be in the pre-slip stage. When $\tau_{yx} > \tau_f$, the structure completely slips and should be in the full-slip stage. Then we discuss the stiffness of the structure at the pre-slip stage and full-slip stage separately.

Under the pre-slip stage, as $\tau_{yx} = \frac{3F}{8b(h_e+h_f)}$ and $\tau_f = \frac{\mu \varepsilon_0 \varepsilon_r U(t)^2}{8{h_f}^2}$, we can obtain the critical load according to $\tau_{yx} \leqslant \tau_f$:

$$F \leqslant \frac{\mu \varepsilon_0 \varepsilon_r b(h_e + h_f)}{3{h_f}^2} U^2 \tag{8}$$

where we assume the voltage is DC, meaning that $U(t) = U$.

By using the Euler–Bernoulli beam theory, we can write the axial strain field in the layers of the flexible parallel electroadhesive structures as:

$$\begin{aligned} \varepsilon_1(x,y) &= -\kappa(x) y \\ \varepsilon_2(x,y) &= -\kappa(x) y \end{aligned} \tag{9}$$

where $\varepsilon_1(x,y)/\varepsilon_2(x,y)$ is the axial strain of the underlying/upper laminate.

The moment-stress relation, which is the governing equation of three-point bending in the pre-slip stage, can be obtained by using the Hooke's law:

$$\begin{aligned} M(x) &= \int_{S_1} -\sigma_1(x,y) y \mathrm{d}S_1 + \int_{S_2} -\sigma_2(x,y) y \mathrm{d}S_2 \\ &= \int_{S_1} -E\varepsilon_1(x,y) y^2 \mathrm{d}S_1 + \int_{S_2} -E\varepsilon_2(x,y) y^2 \mathrm{d}S_2 \\ &= 2\kappa(x) EI \end{aligned} \tag{10}$$

where $\sigma_1(x,y)/\sigma_2(x,y)$ is the axial stress of the underlying/upper laminate andS_1/S_2 is the cross-sectional area of underlying/upper laminate. Note that E here is the combined Young's modulus of the electrodes and insulating materials, then we should calculate E as $E = \frac{E_e h_e + E_f h_f}{h_e + h_f}$.

Boundary conditions of the three-point bending in the pre-slip stage are:

$$\begin{aligned} w(0) = w(L) &= 0 \\ w\left(\frac{L^+}{2}\right) &= w\left(\frac{L^-}{2}\right) \\ \frac{\mathrm{d}w}{\mathrm{d}x}\left(\frac{L^+}{2}\right) &= \frac{\mathrm{d}w}{\mathrm{d}x}\left(\frac{L^-}{2}\right). \end{aligned} \tag{11}$$

Due to the small deformation assumption of Euler–Bernoulli beams, we have $\kappa(x) = \frac{\mathrm{d}^2 w}{\mathrm{d}x^2}$ and $M(x) = 2EI\frac{\mathrm{d}^2 w}{\mathrm{d}x^2}$. The resultant moment is $M(x) = \begin{cases} \frac{1}{2}Fx & 0 < x < \frac{L}{2} \\ \frac{1}{2}F(L-x) & \frac{L}{2} < x < L \end{cases}$, then we have $\frac{\mathrm{d}^2 w}{\mathrm{d}x^2} = \begin{cases} \frac{1}{4EI}Fx & 0 < x < \frac{L}{2} \\ \frac{1}{4EI}F(L-x) & \frac{L}{2} < x < L \end{cases}$ and by integrating it twice and applying the boundary conditions shown in (11), we have:

$$w(x) = \begin{cases} \frac{1}{24EI}Fx^3 - \frac{1}{32EI}FL^2 x & 0 < x < \frac{L}{2} \\ -\frac{1}{24EI}Fx^3 + \frac{1}{8EI}FLx^2 - \frac{3}{32EI}FL^2 x + \frac{1}{96EI}FL^3 & \frac{L}{2} < x < L \end{cases}. \tag{12}$$

Equation (12) is the deflection equation of three-point bending in the pre-slip stage. Substituting (12) into the equation (4) we can have:

$$\frac{1}{k}=-\frac{\partial w}{\partial F}=\begin{cases}-\frac{1}{24EI}x^3+\frac{1}{32EI}L^2x & 0<x<\frac{L}{2}\\ \frac{1}{24EI}x^3-\frac{1}{8EI}Lx^2+\frac{3}{32EI}L^2x-\frac{1}{96EI}L^3 & \frac{L}{2}<x<L\end{cases}.$$

Here we define the ratio of external load to deflection in the middle of the three-point bending model as the stiffness of the structure, then we can get $k=(-\frac{\partial F}{\partial w})_{x=\frac{L}{2}}=\frac{1}{(-\frac{\partial w}{\partial F})_{x=\frac{L}{2}}}=\frac{96EI}{L^3}$. Because $I=\frac{b(h_e+h_f)^3}{3}$ and $E=\frac{E_eh_e+E_fh_f}{h_e+h_f}$, we then have the effective stiffness of three-point bending, which is constant, in the pre-slip stage:

$$k=\frac{32b(E_eh_e+E_fh_f)(h_e+h_f)^2}{L^3}. \tag{13}$$

Under the full-slip stage, we can obtain the critical load according to $\tau_{yx}>\tau_f$ as:

$$F>\frac{\mu\varepsilon_0\varepsilon_r b(h_e+h_f)}{3{h_f}^2}U^2. \tag{14}$$

In slipped sections of the flexible parallel electroadhesive structure, each layer may have a distinct neutral axis, and the location of each neutral axis may vary. Thus, we need to take into account the strain change of the structure due to the position change of the neutral axis. We describe the axial strain field at the bottom and in the top layers as:

$$\begin{aligned}\varepsilon_1(x,y)&=-\kappa(x)y+A_1(x)\\ \varepsilon_2(x,y)&=-\kappa(x)y+A_2(x)\end{aligned} \tag{15}$$

where $A_1(x)/A_2(x)$ is the strain component of the underlying laminate due to the change in the neutral axis position. We then can get the corresponding stress fields: $\begin{cases}\sigma_1(x,y)=E\varepsilon_1(x,y)=-E\kappa(x)y+EA_1(x)\\ \sigma_2(x,y)=E\varepsilon_2(x,y)=-E\kappa(x)y+EA_2(x)\end{cases}$, by using the Hooke's law. Since the parallel electroadhesive structure is not loaded in the axial direction, the integrals of axial stress over any cross-section should be zero. By integrating the corresponding stress fields once and set the result equal to 0, we have $A_1(x)+A_2(x)=0$. Then we have the moment-stress relation:

$$\begin{aligned}M(x)&=\int_{S_1}-\sigma_1(x,y)y\mathrm{d}S_1+\int_{S_2}-\sigma_2(x,y)y\mathrm{d}S_2\\ &=2\kappa(x)EI+2A_1(x)EJ\end{aligned} \tag{16}$$

where J is the first moment of area of a single-layer laminate about the z-axis. We write the static force equilibrium equation of the bottom layer and top layer as:

$$\begin{aligned}-\tau(x)b\mathrm{d}x+\int_{S_1}\sigma_1(x+\mathrm{d}x,y)\mathrm{d}S_1-\int_{S_1}\sigma_1(x,y)\mathrm{d}S_1=0\\ \tau(x)b\mathrm{d}x+\int_{S_2}\sigma_2(x+\mathrm{d}x,y)\mathrm{d}S_2-\int_{S_2}\sigma_2(x,y)\mathrm{d}S_2=0\end{aligned} \tag{17}$$

where $\tau(x)$ is the shear stress exerted by the top surface of the bottom layer onto the bottom surface of the top layer.

In slipped sections of the parallel electroadhesive structure, we have $\tau(x)=\tau_f$. Substituting the corresponding stress fields and $A_1(x)+A_2(x)=0$ into equation (17), we can have:

$$-\tau_f b+EJ\frac{\mathrm{d}\kappa}{\mathrm{d}x}+ES_0\frac{\mathrm{d}A_1}{\mathrm{d}x}=0 \tag{18}$$

where S_0 is the cross-sectional area of a single-layer laminate.

Equations (16) and (18) are the governing equations of three-point bending in the full-slip stage. Apart from the boundary conditions shown in (11), we have an additional boundary condition $\kappa(0)=-\kappa(L)$. Then, the boundary conditions of three-point bending in the full-slip stage are:

$$\begin{aligned}&w(0)=w(L)=0\\ &w\left(\frac{L}{2}^+\right)=w\left(\frac{L}{2}^-\right)\\ &\frac{\mathrm{d}w}{\mathrm{d}x}\left(\frac{L}{2}^+\right)=\frac{\mathrm{d}w}{\mathrm{d}x}\left(\frac{L}{2}^-\right)\\ &\kappa(0)=-\kappa(L).\end{aligned} \tag{19}$$

Because $\kappa(x)=\frac{\mathrm{d}^2w}{\mathrm{d}x^2}$, we have $A_1(x)=\frac{\tau_f b}{ES_0}x-\frac{J}{S_0}\frac{\mathrm{d}^2w}{\mathrm{d}x^2}+C_1$ after integrating the equation (18). Substituting it into equation (16) we can have $M(x)=2E\left(I-\frac{J^2}{S_0}\right)\frac{\mathrm{d}^2w}{\mathrm{d}x^2}+\frac{2J\tau_f b}{S_0}x+2EJC_1$. The resultant moment is $M(x)=\begin{cases}\frac{1}{2}Fx & 0<x<\frac{L}{2}\\ \frac{1}{2}F(L-x) & \frac{L}{2}<x<L\end{cases}$, then we get $\frac{\mathrm{d}^2w}{\mathrm{d}x^2}=\begin{cases}\frac{S_0F-4J\tau_f b}{4E(IS_0-J^2)}x-\frac{JS_0}{IS_0-J^2}C_1 & 0<x<\frac{L}{2}\\ -\frac{S_0F+4J\tau_f b}{4E(IS_0-J^2)}x+\frac{S_0FL}{4E(IS_0-J^2)}-\frac{JS_0}{IS_0-J^2}C_1 & \frac{L}{2}<x<L\end{cases}$ and by integrating it twice and applying the boundary conditions shown in (19), we have the deflection equation of three-point bending in the full-slip stage:

$$w(x)=\begin{cases}\frac{S_0F-4J\tau_f b}{24E(IS_0-J^2)}x^3+\frac{J\tau_f bL}{4E(IS_0-J^2)}x^2-\frac{3S_0FL^2+8J\tau_f bL^2}{96E(IS_0-J^2)}x & 0<x<\frac{L}{2}\\ -\frac{S_0F+4J\tau_f b}{24E(IS_0-J^2)}x^3+\frac{S_0FL+2J\tau_f bL}{8E(IS_0-J^2)}x^2-\frac{9S_0FL^2+8J\tau_f bL^2}{96E(IS_0-J^2)}x & \\ +\frac{S_0FL^3}{96E(IS_0-J^2)} & \frac{L}{2}<x<L\end{cases}. \tag{20}$$

Similar to the pre-slip stage, the effective stiffness of three-point bending, which is also constant, in the full-slip stage is:

$$k=\frac{8b(E_eh_e+E_fh_f)(h_e+h_f)^2}{L^3}. \tag{21}$$

In summary, the stiffness of the three-point bending model at different stages is:

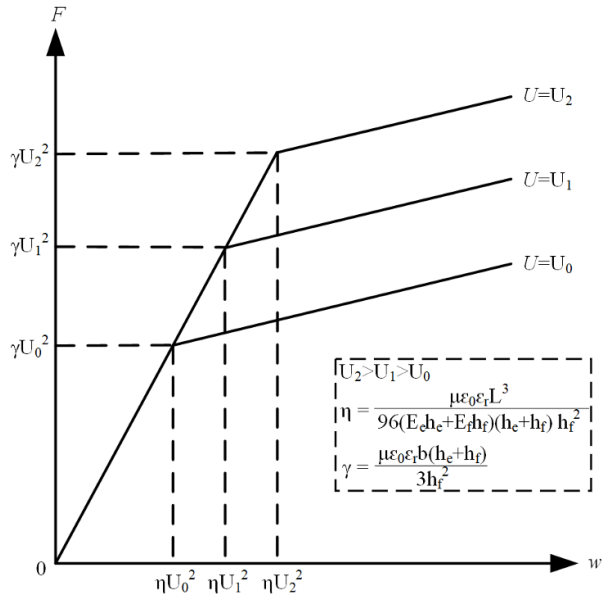

Figure 3. The deflection–force curve of the three-point bending model, where γU_i^2 is the critical load between the pre-slip stage and full-slip stage at different voltages and ηU_i^2 is the corresponding deflections.

$$k = \begin{cases} \dfrac{32b(E_e h_e + E_f h_f)(h_e + h_f)^2}{L^3} & F \leqslant \dfrac{\mu\varepsilon_0\varepsilon_r b(h_e + h_f)}{3{h_f}^2} U^2 \\ \dfrac{8b(E_e h_e + E_f h_f)(h_e + h_f)^2}{L^3} & F > \dfrac{\mu\varepsilon_0\varepsilon_r b(h_e + h_f)}{3{h_f}^2} U^2 \end{cases} \tag{22}$$

The theoretical deflection–force curve of the three-point bending model is shown in figure 3.

2.4. Variable stiffness model of the cantilever beam bending case

2.4.1. Cantilever beams under tip concentrated forces. We then focus on the analytical modelling of cantilever beam bending subjected to tip concentrated forces (see figure 4(a)). In order to determine whether the variable stiffness process has partial-slip or not, we introduce the shear stress calculation equation:

$$\tau_{yx} = \frac{F_S S_z^*}{bI_z} = \frac{3F}{4b(h_e + h_f)}. \tag{23}$$

As the interlaminar shear stress is constant, we have $\tau_{\min} = \tau_{\max} = \tau_{yx}$, then we can conclude that variable stiffness of cantilever beam bending subjected to tip concentrated forces does not have partial-slip stages. When $\tau_{yx} \leqslant \tau_f$, we have $F \leqslant \frac{\mu\varepsilon_0\varepsilon_r b(h_e+h_f)}{6{h_f}^2} U^2$, meaning that the structure is completely adhered together and should be in the pre-slip stage. When $\tau_{yx} > \tau_f$, we have $F > \frac{\mu\varepsilon_0\varepsilon_r b(h_e+h_f)}{6{h_f}^2} U^2$, meaning that the structure completely slips and should be in the full-slip stage.

Since the variable stiffness model derivation process of cantilever beams under tip concentrated forces is similar to the three-point bending model, only the governing equations,

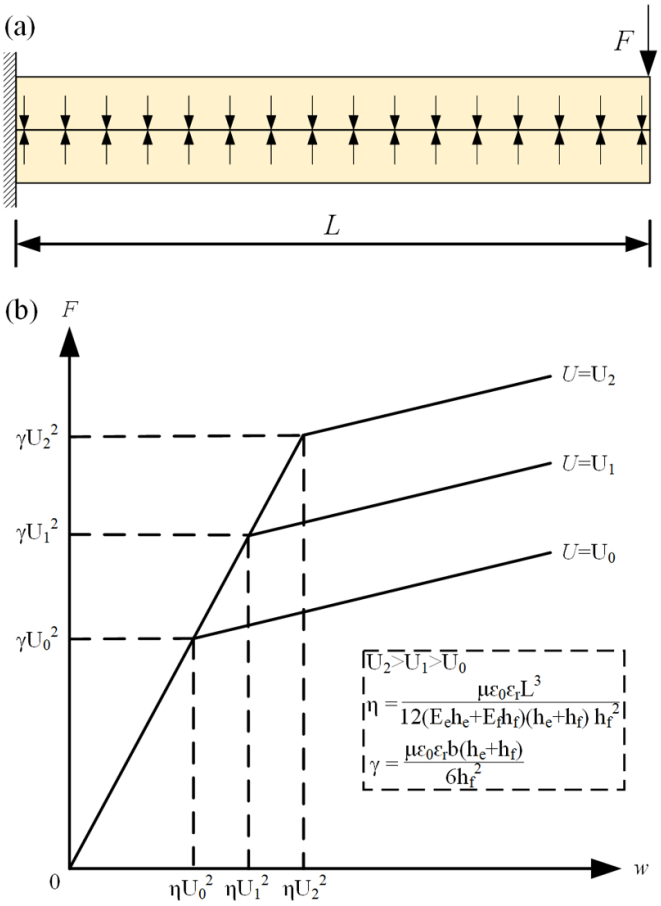

Figure 4. Cantilever beam bending under tip concentrated forces: (a) schematic diagram of the cantilever beam bending under tip concentrated forces, where F is the load and L is the structural length. (b) The deflection–force curve of cantilever beam bending under tip concentrated forces model, where γU_i^2 is the critical load between the pre-slip stage and full-slip stage in different voltage, ηU_i^2 is the corresponding deflection.

boundary conditions, and the final solution are given here (detailed derivation process can be seen in the supplementary material).

Under the pre-slip stage, we have the governing equation:

$$M(x) = 2\kappa(x)EI. \tag{24}$$

Boundary conditions in the pre-slip stage are:

$$\begin{aligned} w(0) &= 0 \\ \frac{\mathrm{d}w}{\mathrm{d}x}(0) &= 0. \end{aligned} \tag{25}$$

Substituting $\kappa(x) = \frac{\mathrm{d}^2 w}{\mathrm{d}x^2}$ and the resultant moment $M(x) = F(x - L)$ into equation (24), and applying the boundary conditions shown in (25), we can have $w(x) = \frac{F}{12EI}x^3 - \frac{FL}{4EI}x^2$. Substituting it into the equation (4) and defining the ratio of external load to deflection in the tip of the cantilever beams under tip concentrated forces model as the stiffness of the structure, we can have the effective stiffness of cantilever beams under tip concentrated forces, which is constant, in the pre-slip stage:

$$k = \frac{2b(E_e h_e + E_f h_f)(h_e + h_f)^2}{L^3}. \tag{26}$$

Under the full-slip stage, we have the governing equation:

$$\begin{aligned} M(x) &= 2\kappa(x)EI + 2A_1(x)EJ \\ &- \tau_f b + EJ\frac{\mathrm{d}\kappa}{\mathrm{d}x} + ES_0\frac{\mathrm{d}A_1}{\mathrm{d}x} = 0. \end{aligned} \tag{27}$$

Boundary conditions in the full-slip stage are:

$$\begin{aligned} w(0) &= 0 \\ \frac{\mathrm{d}w}{\mathrm{d}x}(0) &= 0 \\ \kappa(L) &= 0. \end{aligned} \tag{28}$$

Then we can obtain the stiffness of cantilever beams under tip concentrated forces in the full-slip stage as:

$$k = \frac{b(E_e h_e + E_f h_f)(h_e + h_f)^2}{2L^3}. \tag{29}$$

In summary, the stiffness of the cantilever beam bending under tip concentrated forces model at different stages is:

$$k = \begin{cases} \dfrac{2b(E_e h_e + E_f h_f)(h_e + h_f)^2}{L^3} & F \leqslant \dfrac{\mu\varepsilon_0\varepsilon_r b(h_e + h_f)}{6{h_f}^2}U^2 \\ \dfrac{b(E_e h_e + E_f h_f)(h_e + h_f)^2}{2L^3} & F > \dfrac{\mu\varepsilon_0\varepsilon_r b(h_e + h_f)}{6{h_f}^2}U^2 \end{cases}. \tag{30}$$

The deflection–force curve of cantilever beam bending under tip concentrated forces model is shown in figure 4(b). Detailed deviation of the variable stiffness model of cantilever beams under tip concentrated forces can be seen in the supplementary material.

2.4.2. Cantilever beams under uniformly distributed forces. We then focus on the analytical modelling of cantilever beam bending subjected to uniformly distributed forces (see figure 5(a)). In order to determine whether the variable stiffness process has partial-slip or not, we introduce the shear stress calculation equation:

$$\tau_{yx} = \frac{F_S S_z^*}{bI_z} = \frac{3q(L-x)}{4b(h_e + h_f)}. \tag{31}$$

We can see that the interlaminar shear stress is a changing value: $\tau_{\max} = \tau(0) = \frac{3qL}{4b(h_e+h_f)}$ and $\tau_{\min} = \tau(L) = 0$, which means that there is a condition that $\tau_{\min} < \tau_f \leqslant \tau_{\max}$. Then we can conclude that variable stiffness of cantilever beams under uniformly distributed forces have partial-slip stages, and the slip begins at $x = 0$ position. Thus the whole variable stiffness process involves: (1) the pre-slip stage ($\tau_{\max} \leqslant \tau_f$), (2) the partial-slip stage ($\tau_{\min} < \tau_f \leqslant \tau_{\max}$), and (3) the full-slip stage ($\tau_f < \tau_{\max}$).

Under the pre-slip stage, as $\tau_{\max} \leqslant \tau_f$, we have $q \leqslant \frac{\mu\varepsilon_0\varepsilon_r b(h_e+h_f)}{6Lh_f^2}U^2$, which is the critical load between the pre-slip stage and the partial-slip stage. Similar to the cantilever beam bending subjected to tip concentrated forces, we have the governing equation:

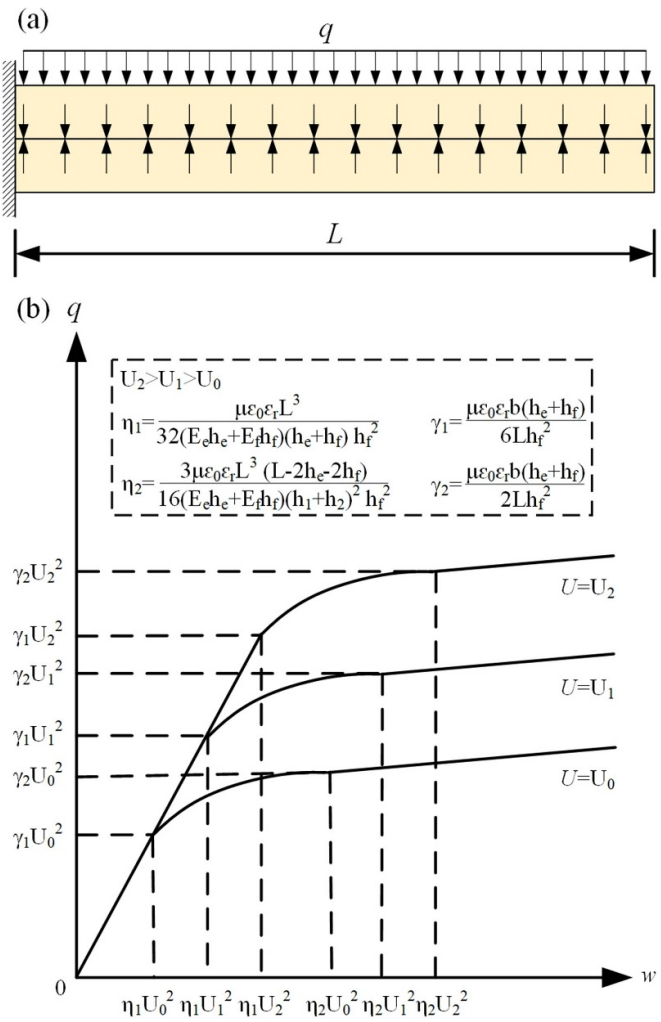

Figure 5. Cantilever beam bending under uniformly distributed forces: (a) schematic diagram of the cantilever beam bending under uniformly distributed forces, where q is the load and L is the structural length. (b) The deflection–force curve of cantilever beam bending under uniformly distributed forces model, where $\gamma_1 U_i^2$ is the critical load between the pre-slip stage and partial-slip stage in different voltage, $\gamma_2 U_i^2$ is the critical load between the partial-slip stage and full-slip stage in different voltage, and $\eta_1 U_i^2/\eta_2 U_i^2$ is the corresponding deflection.

$$M(x) = 2\kappa(x)EI. \tag{32}$$

Boundary conditions in the pre-slip stage are:

$$\begin{aligned} w(0) &= 0 \\ \frac{\mathrm{d}w}{\mathrm{d}x}(0) &= 0. \end{aligned} \tag{33}$$

Substituting $\kappa(x) = \frac{\mathrm{d}^2 w}{\mathrm{d}x^2}$ and the resultant moment $M(x) = -\frac{qL^2}{2} + qLx - \frac{q}{2}x^2$ into equation (32), and applying the boundary conditions shown in (33), we can have $w(x) = -\frac{q}{48EI}x^4 +$

$\frac{qL}{12EI}x^3 - \frac{qL^2}{8EI}x^2$. Substituting it into the equation (4), we can have the effective stiffness of cantilever beam bending subjected to uniformly distributed forces, which is constant, in the pre-slip stage:

$$k = \frac{16b(E_e h_e + E_f h_f)(h_e + h_f)^2}{3L^4}. \tag{34}$$

Under the partial-slip stage, as $\tau_{\min} < \tau_f \leqslant \tau_{\max}$, we have $0 \leqslant \frac{\mu\varepsilon_0\varepsilon_r b(h_e+h_f)}{6Lh_f{}^2}U^2 < q$, which is the critical load between the pre-slip stage and partial-slip stage. Due to the simultaneous existence of slipped sections and cohesive sections in the partial slip stage, we set the χ as the demarcation point between the slipped section and the cohesive section in the partial slip stage. In the slipped section ($0 < x \leqslant \chi$), similar to the cantilever beam bending subjected to tip concentrated forces, we have the governing equation:

$$\begin{aligned} M(x) &= 2\kappa(x)EI + 2A_1(x)EJ \\ &- \tau_f b + EJ\frac{\mathrm{d}\kappa}{\mathrm{d}x} + ES_0\frac{\mathrm{d}A_1}{\mathrm{d}x} = 0. \end{aligned} \tag{35}$$

Boundary conditions of the slipped section in the partial-slip stage are:

$$\begin{aligned} w(0) &= 0 \\ \frac{\mathrm{d}w}{\mathrm{d}x}(0) &= 0. \end{aligned} \tag{36}$$

We then have the continuity conditions:

$$\begin{aligned} w\left(\chi^-\right) &= w\left(\chi^+\right) \\ \frac{\mathrm{d}w}{\mathrm{d}x}\left(\chi^-\right) &= \frac{\mathrm{d}w}{\mathrm{d}x}\left(\chi^+\right) \\ \sigma_1(\chi^-, y) &= \sigma_1(\chi^+, y) \\ \sigma_2(\chi^-, y) &= \sigma_2(\chi^+, y). \end{aligned} \tag{37}$$

Here we set the $\delta(x)$ as the displacement of slipped sections: $\begin{cases} \delta_1(x) = \int A_1(x)\mathrm{d}x \\ \delta_2(x) = \int A_2(x)\mathrm{d}x \end{cases}$, then we have additional continuity conditions:

$$\begin{aligned} \delta_1(\chi^-) &= \delta_1(\chi^+) \\ \delta_2(\chi^-) &= \delta_2(\chi^+). \end{aligned} \tag{38}$$

Substituting $\kappa(x) = \frac{\mathrm{d}^2 w}{\mathrm{d}x^2}$ and the resultant moment $M(x) = -\frac{qL^2}{2} + qLx - \frac{q}{2}x^2$ into equation (35), and applying the boundary conditions shown in (36) and the continuity conditions shown in (37) and (38), we then have $\chi = \frac{3L}{2} - \frac{3\tau_f bI}{qJ}$, which is the demarcation point position and

$$\begin{aligned} w(x) = &-\frac{qS_0}{48E(IS_0 - J^2)}x^4 + \frac{S_0 qL - 2J\tau_f b}{12E(IS_0 - J^2)}x^3 \\ &- \frac{(4q^2 S_0 IL^2 + 12\tau_f{}^2 b^2 I^2 - q^2 L^2 J^2 - 12q\tau_f IbLJ)}{32qIE(IS_0 - J^2)}x^2, \end{aligned}$$

which is the deflection equation of the slipped section of the partial-slip stage.

Under the cohesive section ($\chi < x \leqslant L$), the governing equation is:

$$M(x) = 2\kappa(x)EI. \tag{39}$$

Boundary condition of the cohesive section in the partial-slip stage is:

$$\kappa(L) = 0. \tag{40}$$

Substituting $\kappa(x) = \frac{\mathrm{d}^2 w}{\mathrm{d}x^2}$ and the resultant moment $M(x) = -\frac{qL^2}{2} + qLx - \frac{q}{2}x^2$ into equation (39), and applying the boundary conditions shown in (40) and the continuity conditions shown in (37), we have:

$$\begin{aligned} w(x) = &-\frac{q}{48EI}x^4 + \frac{qL}{12EI}x^3 - \frac{qL^2}{8EI}x^2 + \frac{1}{S_0 I - J^2} \\ &\times \begin{pmatrix} \frac{-9qL^4J^2}{256EI} + \frac{9\tau_f bL^3 J}{32E} - \frac{27(\tau_f bL)^2 I}{32qE} + \frac{9(\tau_f b)^3 LI^2}{8q^2 EJ} \\ -\frac{9(\tau_f b)^4 I^3}{16q^3 EJ^2} \end{pmatrix}, \end{aligned}$$

which is the deflection equation of the cohesive section of the partial-slip stage. Substituting it into the equation (4), we can have the effective stiffness of cantilever beam bending subjected to uniformly distributed forces, which is related to voltage U and load q, in the partial-slip stage:

$$k = \frac{4096b(E_e h_e + E_f h_f)(h_e + h_f)^2 q^4 h_f{}^8}{\begin{bmatrix} 2064q^4 L^4 h_f{}^8 - 216q^2 L^2 b^2 (h_e + h_f)^2 \varepsilon_0{}^2 \varepsilon_r{}^2 U^4 h_f{}^4 + \\ 48qLh_f{}^2 b^3 (h_e + h_f)^3 \varepsilon_0{}^3 \varepsilon_r{}^3 U^6 - 3b^4 (h_e + h_f)^4 \varepsilon_0{}^4 \varepsilon_r{}^4 U^8 \end{bmatrix}}. \tag{41}$$

Under full-slip stage, as $\tau_{\max} < \tau_f$, we can calculate the critical load between the partial-slip stage and the full-slip stage by $L < \chi = \frac{3L}{2} - \frac{3\tau_f bI}{qJ}$ as $q > \frac{\mu\varepsilon_0\varepsilon_r b(h_e+h_f)}{2Lh_2^2}U^2$.

Same as the pre-slip stage, the governing equation is:

$$\begin{aligned} M(x) &= 2\kappa(x)EI + 2A_1(x)EJ \\ &- \tau_f b + EJ\frac{\mathrm{d}\kappa}{\mathrm{d}x} + ES_0\frac{\mathrm{d}A_1}{\mathrm{d}x} = 0. \end{aligned} \tag{42}$$

Boundary condition of the full-slip stage is:

$$\begin{aligned} w(0) &= 0 \\ \frac{\mathrm{d}w}{\mathrm{d}x}(0) &= 0 \\ \kappa(L) &= 0. \end{aligned} \tag{43}$$

Then we can obtain the stiffness of cantilever beams under tip concentrated forces in the full-slip stage as:

$$k = \frac{4b(E_e h_e + E_f h_f)(h_e + h_f)^2}{3L^4}. \tag{44}$$

In summary, the stiffness of the cantilever beam bending under uniformly distributed forces model at different stages is:

$$k=\begin{cases}\dfrac{16b(E_eh_e+E_fh_f)(h_e+h_f)^2}{3L^4} & q\leqslant\dfrac{\mu\varepsilon_0\varepsilon_r b(h_e+h_f)}{6Lh_f{}^2}U^2\\ \dfrac{4096b(E_eh_e+E_fh_f)(h_e+h_f)^2q^4h_f{}^8}{\left[\begin{array}{l}2064q^4L^4h_f{}^8-216q^2L^2b^2(h_e+h_f)^2\varepsilon_0{}^2\varepsilon_r{}^2U^4h_f{}^4\\ +48qLh_f{}^2b^3(h_e+h_f)^3\varepsilon_0{}^3\varepsilon_r{}^3U^6-3b^4(h_e+h_f)^4\varepsilon_0{}^4\varepsilon_r{}^4U^8\end{array}\right]} & \dfrac{\mu\varepsilon_0\varepsilon_r b(h_e+h_f)}{6Lh_f{}^2}U^2<q\leqslant\dfrac{\mu\varepsilon_0\varepsilon_r b(h_e+h_f)}{2Lh_f{}^2}U^2\\ \dfrac{4b(E_eh_e+E_fh_f)(h_e+h_f)^2}{3L^4} & q>\dfrac{\mu\varepsilon_0\varepsilon_r b(h_e+h_f)}{2Lh_f{}^2}U^2\end{cases}. \tag{45}$$

The deflection–force curve of cantilever beam bending under uniformly distributed forces model is shown in figure 5(b). Detailed derivation of the variable stiffness model of cantilever beams under uniformly distributed forces can be seen in the supplementary material.

3. Results and discussions

For the parallel electroadhesive structure, we can see from figures 3 and 4 that, for both the three-point bending case and the cantilever beam bending case under tip concentrated forces: (1) we only see pre-slip and full-slip during bending; (2) the stiffness during the pre-slip stage is four times larger than the stiffness in the full-slip stage; and (3) increasing the voltage, dielectric permittivity and the coefficient of friction can both elongate the pre-slip stage, thus can enhance the structural load capability. As for the cantilever beam bending case under uniformly distributed forces (see figure 5), the stiffness change is the same four times between pre-slip and full-slip and increasing the voltage can also enhance the structural load capability. However, there is a partial-slip stage between the pre-slip and full-slip. In this stage, layer slip began at the fixed end of the cantilever beam and extended along the axial direction until the demarcation point $x=\chi$ between the slipped section and the cohesive section in the partial slip stage exceeded $x=L$, and then entered into the full slip stage. The position and movement of χ, related to the applied voltage, had a large effect on the structure stiffness change in this stage. So varying the voltage between the partial-slip stage can modulate the overall structural stiffness change.

To validate the model of three-point beam bending, we developed a three-point bending experimental setup based on a tensile testing machine (SBA-10, Chongqing Hacco Technology Co., Ltd). The schematic diagram of the setup is shown in the inlet in figure 6(a). The electroadhesive pad was made of chemical etching unwanted copper area (thickness of 17 μm and elastic modulus of 108 GPa) on a polyimide (PI) film (thickness of 52 μm, elastic modulus of 3.801 GPa, and relative permittivity of 3.5). The film area was 50 mm × 80 mm and the effective electrode area was 40 mm × 60 mm. The static coefficient of friction between two PI films under the application of 2 kV was 3.06. The support span length was 34 mm.

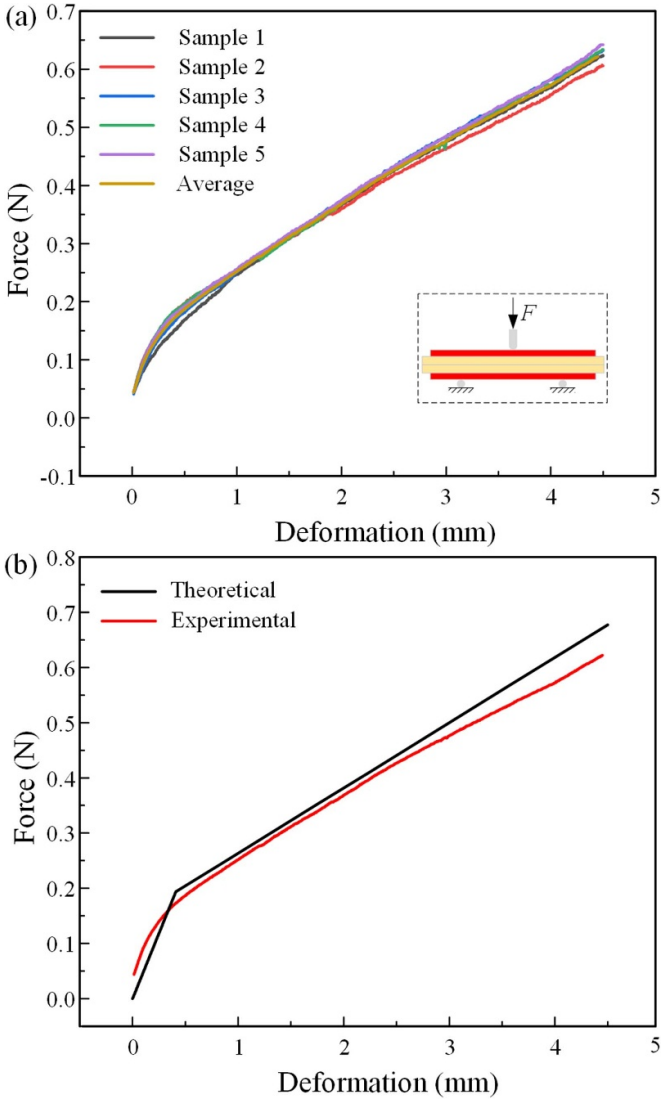

Figure 6. Three-point beam bending model validation: (a) experimental data of five different samples and (b) comparison between the theoretical and experimental deflection–force curve of the three-point beam bending case.

We applied 2 kV to the electrodes for 10 s and then we moved down the tensile machine in a speed of 6 mm min^{-1}. We started recording the deformation when there was a 0.04 N load.

We fabricated and tested five samples. It is clear from figure 6(a) that the deviation between different samples was minor. We then used the experimental average to compare with the theoretical result. As shown in figure 6(b), the theoretical deflection–force curve agreed relatively well with the experimental curve, both showing a clear similar transition between pre-slip to full-slip. Minor deviations may mainly due to the small air gaps between the parallel electroadhesive structure and these air gaps could lead to imperfect contacts thus partial adhesion between layers, resulting 'fake' partial slips as shown in the experimental results. In the theoretical model, however, as air was not included, the lines were perfect and straight.

To validate the model of cantilever beam bending under tip concentrated force, we employed the same EA structure as the

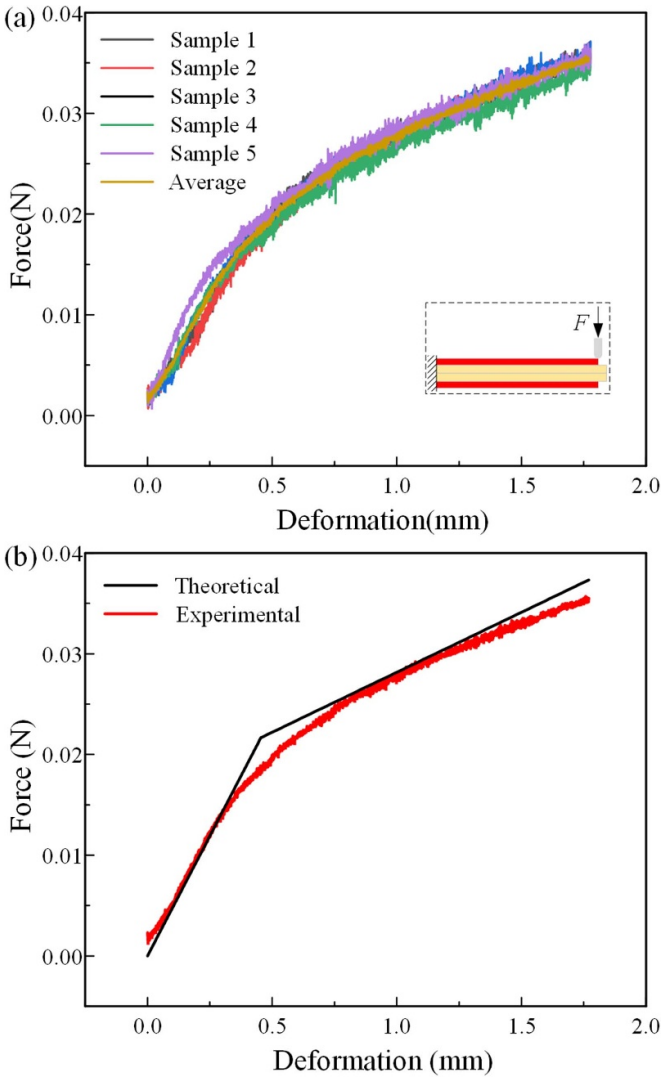

Figure 7. Cantilever beam under tip concentrated forces bending model validation: (a) experimental data of five different samples and (b) comparison between the theoretical and experimental deflection–force curve of the cantilever beam bending under tip concentrated forces case.

model of three-point bending. It is worth noting that, due to the low load-bearing and large deformation characteristics of the cantilever beam structure itself, we need to find more precise force sensors to detect the load and apply a lower voltage to ensure that it can complete the two processes of adsorption and slip timely within a small deformation. Therefore, we developed a cantilever beam bending experimental setup based on an electric universal testing machine (AGS-X-10kN, Shimadzu Instruments Manufacturing, Co., Ltd) with better force readings. The schematic diagram of the setup is shown in the inlet in figure 7(a). We conducted the verification experiments using 1 kV. The static coefficient of friction between two PI films under the application of 1 kV was 2.74. The support span length was 29 mm. We applied 1 kV to the electrodes for 10 s and then moved down the tensile machine in a speed of 2 mm min^{-1}. We started recording the deformation when there was a 0.002 N load.

It is also clear from figure 7(a) that the deviation between five different samples was minor. The data in figure 7(a) have more noise than the data shown in figure 6(a) as we used a force sensor with a higher resolution. As shown in figure 7(b), we can see that the theoretical deflection–force curve of cantilever beam bending under tip concentrated force also agreed relatively well with the experimental curve, both showing clearly similar trends in pre-slip and full-slip. The reason for the slight deviation is the same as the three-point bending experiment, probably mainly due to the small air gaps between the parallel electroadhesive structures, which can lead to imperfect contacts and thus 'false' partial slips. The reason why the theoretical line is straight is due to the fact that the model does not consider air between layers. Validating the model of cantilever beam bending under uniformly distributed forces will be completed in the future as it is currently challenging to establish a decent and convincing experimental setup.

4. Conclusion and future work

In this work, we have developed the first comprehensive analytical variable stiffness model of flexible parallel electroadhesive structures. By combining the Euler–Bernoulli beam theory with the Maxwell stress tensor, together with considering frictions and slips between two layers, the model has considered three different conditions: three-point bending, cantilever beam bending subjected to tip concentrated forces, and cantilever beam bending subjected to uniformly distributed forces. The model has also considered the actual electrode thickness and its Young's modulus.

Key findings of this work include that: (1) three-point bending and cantilever beam bending under tip concentrated forces only have pre-slip and full-slip, whereas cantilever beam bending under uniformly distributed forces has an additional partial-slip which can be used for stiffness modulation; (2) the reason leads to partial-slips comes from changed shear force distributions inside structures; so for any electrostatic jamming structures that are subjected to area loads, partial-slips will occur. (3) The stiffness during the pre-slip stage is four times larger than the stiffness in the full-slip stage; (4) increasing the voltage, dielectric permittivity and coefficient of friction can elongate the pre-slip stage, thus enhancing the structural load capability. The findings are useful insights towards further understanding of the variable stiffness mechanism of electroadhesive layer jamming.

Both the theoretical deflection–force curve regarding the three-point bending case and cantilever beam bending under tip concentrated forces agreed relatively well with their experimental ones, showing the effectiveness of the model and the good repeatability of our EA fabrication. The model and the results are helpful for parallel electroadhesive jamming structural optimization for stiffness tuning applications. Future work include but is not limited to: (1) the investigation into how different electrode/dielectric thickness and their electrical properties influence the structural variable stiffness effect, (2) experimental validation of the model of cantilever beam bending under uniformly distributed forces, and (3) variable

stiffness modelling multi-layer flexible electroadhesive jamming structures.

Data availability statement

All data that support the findings of this study are included within the article (and any supplementary files).

Acknowledgments

We thank Professor Fei Jia for helpful discussions. This work was supported by the Scientific Research Foundation for High-level Talents at Shenzhen (Grant No. ZX20210144), and the National Natural Science Foundation of China (Grant No. 12102106).

ORCID iDs

Yingze Yuan https://orcid.org/0000-0002-8587-3227
Jianglong Guo https://orcid.org/0000-0002-9997-6059
Liwu Liu https://orcid.org/0000-0002-7737-9827
Yanju Liu https://orcid.org/0000-0001-8269-1594
Jinsong Leng https://orcid.org/0000-0001-5098-9871

References

[1] Saavedra Flores E I, Friswell M I and Xia Y 2013 Variable stiffness biological and bio-inspired materials *J. Intell. Mater. Syst. Struct.* **24** 529–40
[2] Kuder I K, Arrieta A F, Raither W E and Ermanni P 2013 Variable stiffness material and structural concepts for morphing applications *Prog. Aerosp. Sci.* **63** 33–55
[3] Manti M, Cacucciolo V and Cianchetti M 2016 Stiffening in soft robotics: a review of the state of the art *IEEE Robot. Autom. Mag.* **23** 93–106
[4] Wang L, Yang Y, Chen Y, Majidi C, Iida F, Askounis E and Pei Q 2018 Controllable and reversible tuning of material rigidity for robot applications *Mater. Today* **21** 563–76
[5] Wang H, Chen S, Zhu X, Yuan B, Sun X, Zhang J, Yang X, Wei Y and Liu J 2022 Phase transition science and engineering of gallium-based liquid metal *Matter* **5** 2054–85
[6] Hao Y, Gao J, Lv Y and Liu J 2022 Low melting point alloys enabled stiffness tunable advanced materials *Adv. Funct. Mater.* **32** 2201942
[7] Fitzgerald S G, Delaney G W and Howard D 2020 A review of jamming actuation in soft robotics *Actuators* **9** 104
[8] Brown E, Rodenberg N, Amend J, Mozeika A, Steltz E, Zakin M R, Lipson H and Jaeger H M 2010 Universal robotic gripper based on the jamming of granular material *Proc. Natl Acad. Sci.* **107** 18809–14
[9] Amend J R, Brown E, Rodenberg N, Jaeger H M and Lipson H 2012 A positive pressure universal gripper based on the jamming of granular material *IEEE Trans. Robot.* **28** 341–50
[10] Ibrahimi M, Paternò L, Ricotti L and Menciassi A 2021 A layer jamming actuator for tunable stiffness and shape-changing devices *Soft Robot.* **8** 85–96
[11] Narang Y S, Vlassak J J and Howe R D 2018 Mechanically versatile soft machines through laminar jamming *Adv. Funct. Mater.* **28** 1707136
[12] Tadakuma K, Fujimoto T, Watanabe M, Shimizu T, Takane E, Konyo M and Tadokoro S 2020 Fire-resistant deformable soft gripper based on wire jamming mechanism *3rd IEEE Int. Conf. on Soft Robotics* pp 740–7
[13] Brancadoro M, Manti M, Tognarelli S and Cianchetti M 2020 Fiber jamming transition as a stiffening mechanism for soft robotics *Soft Robot.* **7** 663–74
[14] Wang T, Zhang J, Li Y, Hong J and Wang M Y 2019 Electrostatic layer jamming variable stiffness for soft robotics *IEEE/ASME Trans. Mechatronics* **24** 424–33
[15] Bergamini A, Christen R and Motavalli M 2007 Electrostatically tunable bending stiffness in a GFRP–CFRP composite beam *Smart Mater. Struct.* **16** 575
[16] Imamura H, Kadooka K and Taya M 2017 A variable stiffness dielectric elastomer actuator based on electrostatic chucking *Soft Matter* **13** 3440–8
[17] Henke M and Gerlach G 2014 On a high-potential variable-stiffness device *Microsyst. Technol.* **20** 599–606
[18] Tabata O, Konishi S, Cusin P, Ito Y, Kawai F, Hirai S and Kawamura S 2001 Micro fabricated tunable bending stiffness devices *Sens. Actuator* A **89** 119–23
[19] Griffiths D J Reed College and Oregon 2017 *Introduction to Electrodynamics* 4th edn (Cam: CUP) p 362
[20] Di Lillo L, Raither W, Bergamini A, Zündel M and Ermanni P 2013 Tuning the mechanical behaviour of structural elements by electric fields *Appl. Phys. Lett.* **102** 224106
[21] García-Berríos E, Gao T, Woodka M D, Maldonado S, Brunschwig B S, Ellsworth M W and Lewis N S 2010 Response versus chain length of alkanethiol-capped Au nanoparticle chemiresistive chemical vapor sensors *J. Phys. Chem.* C **114** 21914–20